

Ultrafast All-Optical Measurement of Squeezed Vacuum in a Lithium Niobate Nanophotonic Circuit

James Williams^{1,†}, Elina Sendonaris^{2,†}, Rajveer Nehra^{1,3,4,5},
Robert M Gray¹, Ryoto Sekine¹, Luis Ledezma¹, Alireza Marandi^{1,2*}

¹ *Department of Electrical Engineering, California Institute of Technology, Pasadena, California 91125*

² *Department of Applied Physics, California Institute of Technology, Pasadena, California 91125*

³ *Department of Electrical and Computer Engineering,
University of Massachusetts Amherst, Amherst, Massachusetts 01003, USA*

⁴ *Department of Physics, University of Massachusetts Amherst, Amherst, Massachusetts 01003, USA*

⁵ *College of Information and Computer Science, University of
Massachusetts Amherst, Amherst, Massachusetts 01003, USA*

[†] *These authors contributed equally.*

Squeezed vacuum, a fundamental resource for continuous-variable quantum information processing, has been used to demonstrate quantum advantages in sensing, communication, and computation. While most experiments use homodyne detection to characterize squeezing and are therefore limited to electronic bandwidths, recent experiments have shown optical parametric amplification (OPA) to be a viable measurement strategy. Here, we realize OPA-based quantum state tomography in integrated photonics and demonstrate the generation and all-optical Wigner tomography of squeezed vacuum in a nanophotonic circuit. We employ dispersion engineering to enable the distortion-free propagation of femtosecond pulses and achieve ultrabroad operation bandwidths, effectively lifting the speed restrictions imposed by traditional electronics on quantum measurements with a theoretical maximum clock speed of 6.5 THz. We implement our circuit on thin-film lithium niobate, a platform compatible with a wide variety of active and passive photonic components. Our results chart a course for realizing all-optical ultrafast quantum information processing in an integrated room-temperature platform.

I. INTRODUCTION

Many quantum systems have been used to gain an advantage over otherwise purely classical means in a variety of fields [1–3]. Implementations of provably-secure quantum key distribution and random-number generation are now commercially available [4–6]. Many enhanced sensing techniques using squeezed and non-classical states of light with applications in chemistry and imaging have been shown [7–10]. Considerable effort is currently being invested into building quantum computers both in research and industry [11–13].

Photonics has emerged as a front-runner for quantum information processing for several key reasons. Most photonic technologies are capable of operating at room temperature outside a carefully controlled cryogenic environment. Advances in integrated photonics have allowed many devices and circuits to be combined into a single monolithic platform similar to CMOS technology and the advent of integrated circuits [14]. Photonics also offers an inherently broad bandwidth which, when combined with dispersion engineering, can allow for the manipulation and propagation of ultra-short pulses of light [15]. Time-multiplexing, an effective technique used in photonic systems to increase information throughput [16–18], can leverage femtosecond pulses to achieve clock speeds

far exceeding what is currently possible with conventional electronics.

Optical parametric amplifiers (OPAs) are a cornerstone of quantum optics and continuous-variable quantum information, and have been studied extensively in a variety of different contexts. In the low-gain limit, OPAs generate pairs of entangled photons for quantum-enhanced sensing and quantum key distribution [19–23]. Boson sampling with a quantum advantage has recently been demonstrated with 100 independent OPAs [24]. At higher gains, OPAs generate squeezed vacuum (SV), a quantum state in which one quadrature is compressed below the shot-noise limit. SV is often used for sensing enhancement [25] and most notably in the LIGO experiment [26]. Independently-generated SV states can be combined to create a highly entangled cluster state for universal quantum computation [27, 28]. SV generation from a type-0 source is typically spectro-temporally multimode. Recently, several experiments have demonstrated how these modes can be utilized as a basis for quantum information. Bulk experiments have shown that shaping the spectral profile of the pump can control the occupancy of each mode [29]. Pump shaping combined with engineering of the phase matching condition for sum-frequency generation can be used to isolate and measure each individual mode [30, 31].

A crucial part of any quantum information processing system is a measurement device capable of characterizing a component of interest. For SV, homodyne detection is often employed as its phase-sensitive nature can be used

* marandi@caltech.edu

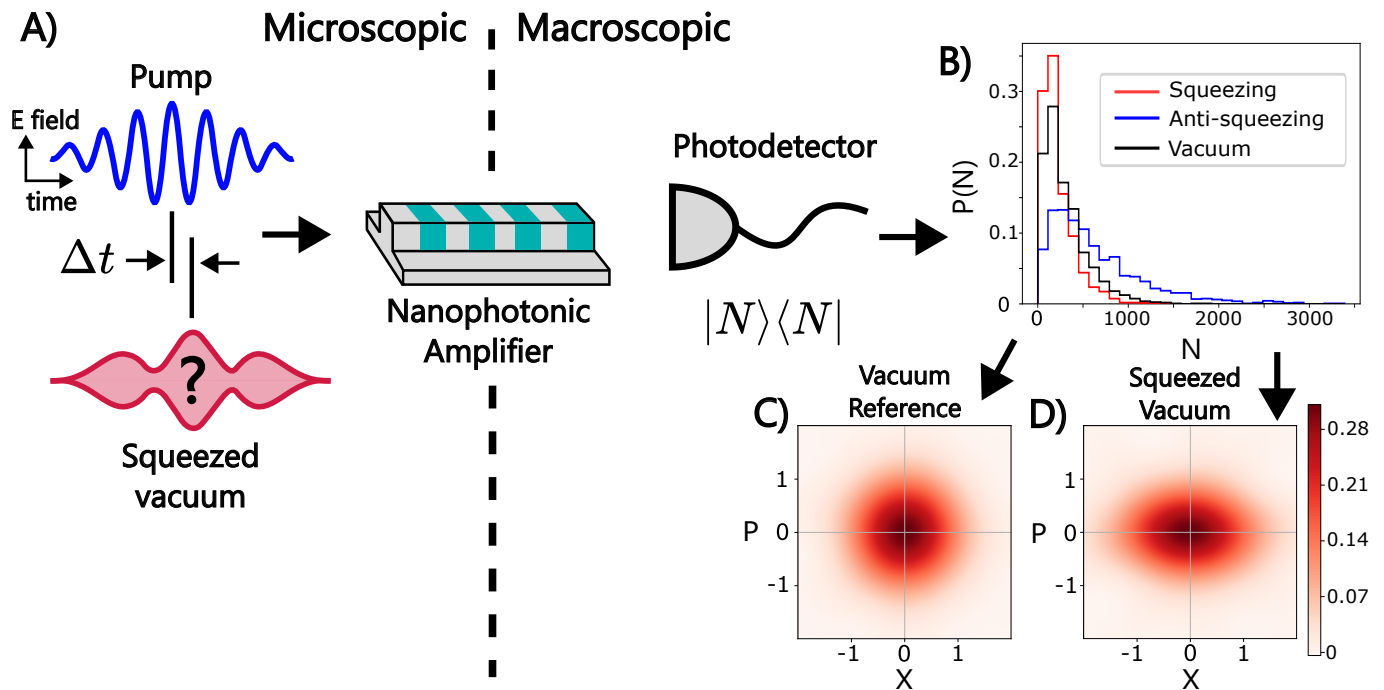


FIG. 1. A) Layout of the measurement procedure. Δt represents the relative time-delay between the pump and squeezed vacuum where a 0.775 fs delay corresponds to a measurement phase of $\phi = \frac{\pi}{2}$. B) Measured photon number distributions for squeezing ($\phi = \frac{\pi}{2}$), anti-squeezing ($\phi = 0$) and vacuum. C) Wigner function recovered for vacuum. D) Wigner function recovered for squeezed vacuum.

to reconstruct the Wigner function, a quasi-probability distribution over two non-commuting quadratures which completely characterizes a quantum state. Homodyne detectors can isolate a single mode by shaping the spectral profile of the pump appropriately [32]. This phase-sensitive and mode-selective behavior makes them well-suited for characterizing a variety of quantum states, including non-classical states. Single-photon and photon number-resolving (PNR) detectors are also common tools for state characterization, especially in the context of states exhibiting Wigner negativity [33, 34]. Given the non-Gaussian nature of their measurement operator, PNR detectors have been used to generate non-classical states which are characterized through homodyne detection [35–38]. While homodyne and PNR detection are powerful techniques for probing quantum states of interest, their speed is ultimately constrained by the bandwidth of the electronics used to physically realize these detectors, which are limited to the GHz range.

OPAs have seen use as a method of measuring quantum information [39, 40]. Degenerate $\chi^{(2)}$ OPAs use a non-linear medium to amplify a signal at ω using a pump at 2ω . Importantly, OPAs amplify the portion of the signal that is in-phase with the pump and de-amplify the out-of-phase portion. Similar to homodyne detection, this phase sensitivity allows for quantum information to be recovered from the input state by resolving the number of photons in the output state [41, 42].

Here, we demonstrate OPA-based Wigner tomogra-

phy in lithium niobate nanophotonics. In our previous demonstration of nanophotonic OPA measurements [41], we measured the average photon number at the output of the OPA to calculate squeezing levels. In this work, we use a fast photodetector to measure each pulse and resolve the statistical information necessary to calculate the Wigner function of the input SV. Our OPA has low dispersion at both the pump and signal wavelengths, allowing for the distortion-free propagation and amplification of femtosecond pulses. Such an OPA-based circuit for generating and measuring SV supports a maximum clock speed of 6.5 THz for time-multiplexed quantum information processing. Our results highlight nanophotonic OPAs as an important building block for ultrafast quantum state measurement and information processing on a chip and at room temperature.

II. PARAMETRIC AMPLIFIERS AS QUANTUM MEASUREMENT DEVICES

Early proposals of OPAs as quantum measurement devices demonstrated loss tolerance and detector inefficiency mitigation [43]. OPAs are particularly well-suited for this task as their phase-sensitive amplification is in principle noiseless unlike phase-insensitive amplifiers such as erbium-doped fibers and semiconductor gain media [44]. OPA-assisted balanced homodyne detection has been used to characterize fiber-based sources

of SV over 43 GHz of electronic bandwidth [45]. A similar technique has also been demonstrated using the $\chi^{(3)}$ nonlinearity [40]. Other experiments have shown quantum-enhanced sensing using an SU(1,1) interferometer constructed from two OPAs for state readout [46, 47]. OPAs have also been used to amplify weak spatially-varying signals and detect quantum correlations for imaging applications [48, 49]. All-optical feed-forward, a technique used to surpass the constraints of electronics in feed-forward schemes for quantum information processing, has been demonstrated using 3 OPAs [50]. Wigner-tomography of squeezed states using bulk OPAs has been experimentally realized [42]. OPA-based techniques have also been extended to squeezing across multiple spatial modes where direct detection is used to disentangle and analyze each mode independently [51].

A. Quadrature Measurement

Figure 1 depicts the scheme used to measure the Wigner function of a squeezed vacuum state. When a quantum signal enters the OPA, its in-phase quadrature \hat{x}_ϕ is amplified by the pump while its out-of-phase quadrature \hat{p}_ϕ is deamplified. These quadratures map to the original operators of the state as [42]:

$$\hat{x}_\phi = \hat{x}\cos(\phi) + \hat{p}\sin(\phi) \quad (1)$$

$$\hat{p}_\phi = \hat{p}\cos(\phi) - \hat{x}\sin(\phi) \quad (2)$$

Where ϕ represents a relative phase between the pump and amplified signal induced by adjusting the time-delay (Δt) of the pump. After amplification, the output quadratures can be expressed as:

$$\hat{X}_\phi = \hat{x}_\phi e^g \quad (3)$$

$$\hat{P}_\phi = \hat{p}_\phi e^{-g} \quad (4)$$

where e^g , the gain of the amplifier, can be controlled by changing the pump power. The operator for the number of photons in the signal field at the output is then:

$$\hat{N}_\phi = \hat{X}_\phi^2 + \hat{P}_\phi^2 - \frac{1}{2} \quad (5)$$

For a large gain, the 2nd and 3rd terms of Eq.5 can be ignored such that:

$$\hat{N}_\phi \approx \hat{X}_\phi^2 \quad (6)$$

By resolving the number of photons at the output of the OPA in the signal field in each pulse, we can recover the marginal distribution $P(N, \phi)$, or the probability of detecting N photons at a pump phase ϕ .

Because our OPA exhibits low dispersion over a broad bandwidth while operating in the type-0 phase matching configuration, it amplifies many orthogonal spectrotemporal modes simultaneously [52], all of which contribute to the measured $P(N, \phi)$. These modes can be

calculated analytically by computing the joint spectral intensity (JSI) function of the signal and idler. Our JSI and the corresponding modes are computed and plotted in the supplementary using the dispersion parameters calculated from the waveguide geometry and the Heisenberg propagators derived in [53]. As our JSI is inseparable ($JSI(\omega_s, \omega_i) \neq \phi(\omega_s)\phi(\omega_i)$), it is composed of multiple independent modes $\Phi(\omega_s, \omega_i)$ of the form $\Phi(\omega_s, \omega_i) = \phi(\omega_s)\phi(\omega_i)$.

At the photodetector, we use a combination of a 1700-nm long-pass filter and 1950-nm short-pass filter to suppress contributions from higher order modes. Using the measured $P(N)$ for vacuum amplification (i.e when no signal field is sent into the OPA), we calculate a Schmidt number of 1.35 modes using definition of $g^{(2)}$ from [54]. Contributions from the higher-order modes are quantified and separated by fitting a 2-mode photon number distribution to determine the gain of the fundamental mode as a function of ϕ . For a single mode, the photon number distribution is

$$P_{\langle N \rangle}^1(N, r) = \frac{1}{\sqrt{2\pi N \langle N \rangle(r)}} e^{-\frac{N}{2\langle N \rangle(r)}} \quad (7)$$

where $\langle N \rangle(r)$ is the squeezing-dependent average photon number. Convoluting this distribution with itself yields the 2-mode distribution [55]:

$$P^2(N, r) = \int_0^\infty P_{\langle N_1 \rangle}^1(N - n, r) P_{\langle N_2 \rangle}^1(n, r) dn \quad (8)$$

Intuitively, this convolution can be understood as a sum of all probabilities for which the photon contributions of the first and second modes sum to N as the photodetector cannot distinguish between photons arriving from different modes. These fitted distributions are then sampled and used as inputs to a maximum-likelihood reconstruction algorithm to recover the density matrix and Wigner function [56].

B. Dispersion Engineering

A key advantage of using nanophotonics is the ability to control the dispersive properties of the waveguides used to create photonic circuits. Figure 2 depicts our ridge waveguide geometry and material stack used for our OPAs. We fabricate our OPAs on a thin-film lithium niobate (TFLN) on silica on silicon wafers available from NanoLN. By adjusting the width, height and etch depth of the waveguide, we can manipulate its dispersive properties to achieve low group velocity dispersion (GVM) at the pump and signal wavelengths while simultaneously minimizing the walk-off from group velocity mismatch (GVM) between the pump and signal [15]. This regime of operation allows for our OPA to exhibit high gain over a broad bandwidth, making it an

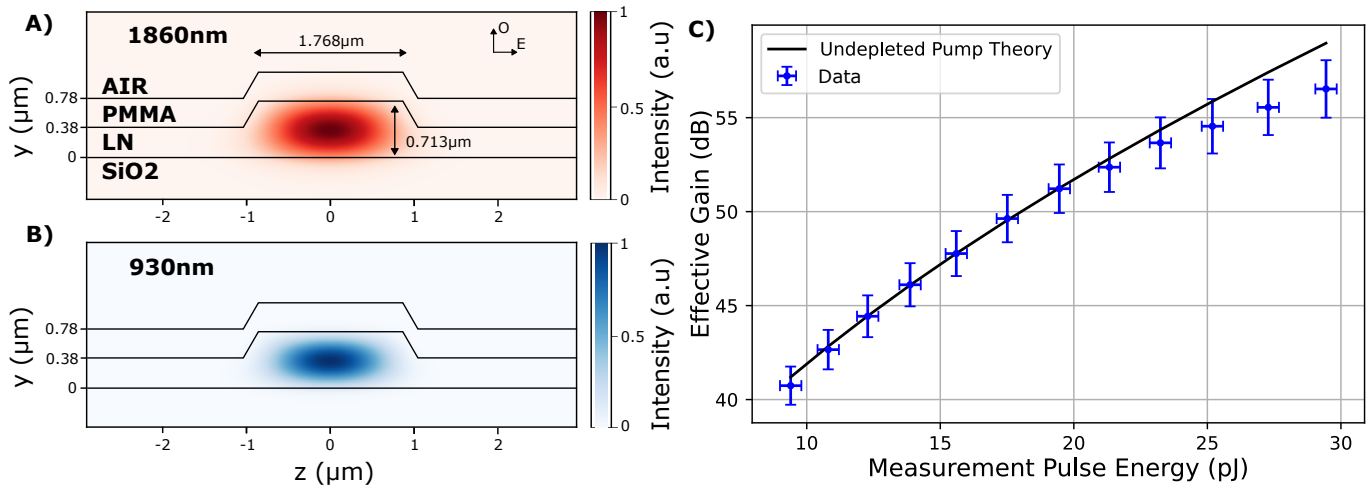


FIG. 2. A) Signal spatial mode within our waveguide. Text on the right denotes the material stack-up with air, poly methyl methacrylate (PMMA), lithium niobate (LN) and silicon dioxide (SiO₂). Dimensions are indicated by the vertical and horizontal measurements. The ordinary and extraordinary crystal axes are denoted at the top right. B) Pump spatial mode. C) OPA gain vs measurement pump energy. Error bars are calculated from pump and signal coupling stability measurements taken before gain measurements.

ideal tool for studying quantum states encoded in ultrafast pulses. Our waveguide geometry achieves a GVD of $-17.3 \text{ fs}^2/\text{mm}$ at our signal wavelength of 1860 nm, $244 \text{ fs}^2/\text{mm}$ at our pump wavelength of 930 nm, and a GVM of $-87 \text{ fs}/\text{mm}$. By comparison, bulk lithium niobate has a GVD of $13.3 \text{ fs}^2/\text{mm}$ at 1860 nm, a GVD of $341 \text{ fs}^2/\text{mm}$ at 930 nm, and a GVM of $203 \text{ fs}/\text{mm}$. A thin layer of poly-methyl methacrylate (PMMA) is deposited via spin-coating on top of the waveguide to tune the phase matching condition. We note that our design is not perfectly optimal, and that geometries with lower dispersion have been demonstrated [15].

Operating with low dispersion allows us to utilize ultrafast femtosecond pulses at both the pump and signal frequencies. Shorter pulses are advantageous in nonlinear optics as the high peak power from temporal confinement can achieve a stronger nonlinear interaction for the same pulse energy. This interaction is also enhanced by the tight spatial mode confinement offered by ridge waveguides. Furthermore, by shortening the length of the pump and signal pulses in the time domain, subsequent pulses can be packed closer together in time, enabling a significant boost in clock speeds for time-multiplexing. Based on the dispersive properties of our 5-mm measurement OPA and our 70-fs pump source, we estimate an upper bound on the temporal length of our SV of 154.3 fs, which gives a theoretical maximum of 6.5 THz for our clock rate [57]. This clock rate can be increased further by using a shorter OPA and a higher pump power, or more advanced dispersion engineering.

Dispersion engineering in TFLN has been used to demonstrate broadband amplifiers with record-breaking gain bandwidths [15]. Dispersion-engineered OPAs have been shown to be suitable devices for both generating and measuring the time-averaged squeezing of SV [41] as

well as producing short-pulse biphotons [58]. Ultrafast switching [59], and ultrafast computation of nonlinear functions for machine learning have been achieved [60]. Combining these OPAs with resonators has allowed new regimes of nonlinearity to be studied which were previously impossible to achieve in bulk platforms [61].

C. Pump Depletion

An important consideration for OPAs as quantum measurement devices is the depletion experienced by the pump during amplification. As the pump energy increases, the nonlinear interaction becomes more efficient, causing the pump pulse to deplete while propagating in the OPA and the gain to saturate. Figure 2C shows measured on-chip OPA gain vs the input pump energy. The black line represents the theoretical undepleted pump gain $G_{dB} = 10 \log_{10}(e^{b\sqrt{E}})$ where E is the pump energy in Joules and b is a found by fitting the pump energy vs gain curve in the undepleted regime. Around 20 pJ, the measured gain begins to saturate relative to the theoretical gain due to pump depletion effects.

Pump depletion impacts our measurement in two ways. First, the larger photon number components of the state being measured experience less gain than smaller photon number components. This phenomenon, often known as gain saturation for classical amplifiers, suppresses the larger photon number contributions to the measured photon number distribution. Second, pump depletion can be thought of as a semi-deterministic transfer of energy from the pump pulse to the signal pulse. This causes the peak of the photon number distribution to shift away from $N = 0$. We observe this effect in classical simulations which use a split-step Fourier method to simulate single-

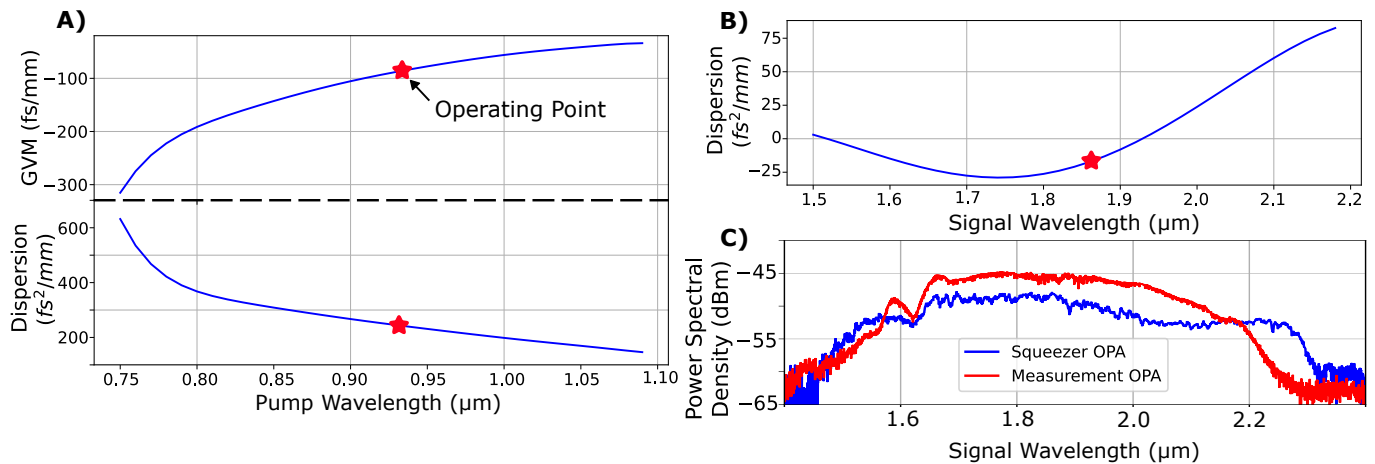


FIG. 3. A) Pump dispersion and group-velocity mismatch (calculated at degeneracy and plotted at the pump wavelength) for our OPA. B) Signal dispersion vs wavelength. C) Parametric generation (vacuum amplification) spectra of our measurement and squeezer OPAs.

mode and multimode vacuum measurements. These simulations are detailed in the supplementary. This effect has also been observed in single-mode quantum simulations [62] and experimentally [54]. We address this issue when fitting our data with 2-mode distributions by fitting a constant offset along the N axis, leading to good agreement between the measured data and fitted distributions.

III. EXPERIMENTAL SETUP

Figure 4 shows the experimental setup. An 80 MHz mode-locked titanium-sapphire laser (MLL) sends 70-fs pulses to a half-wave plate (HWP) and polarizing beam-splitter (PBS) combination to control the power splitting between the measurement and squeezer beam paths. Pump light for the squeezer OPA is sent to a delay stage used to scan ϕ in equation 1. A shutter is also placed in this path to block the squeezer beam for shot-noise calibration. Two continuously variable neutral density filters (VND) are used in both paths to fine tune the input power. The paths are combined on a reflective objective (Obj) and focused onto the waveguide inputs for the OPAs. Figure 4A shows the layout of the nanophotonic circuit. In the squeezer OPA, the vacuum field around 1860 nm is squeezed by the pump. The SV and the remaining pump light enter an adiabatic coupler which passes at least 55% of the SV and 5% of the pump into the measurement OPA. Inside the measurement OPA, the SV is amplified by a strong pump pulse (40 pJ) to macroscopic photon levels detectable by a fast photodetector. A lensed fiber collects light from the output of the measurement OPA and directs it to a series of free-space filters used to remove remaining pump light, including the previously mentioned 1700-nm long pass and a 1950-nm short pass for limiting the measured mode number. From here, the filtered SV is collected into single-mode

fiber and enters a 90/10 splitter where 90% is sent to a fast (10 GHz) photodetector and fast (80 GSFS 40 GHz) oscilloscope used to resolve individual pulses while the remaining 10% is sent to a slow (1MHz) detector and slow (100 MSPS 10 MHz) oscilloscope used to detect the amplification fringe and determine the measurement phase ϕ .

IV. DATA ANALYSIS

A. Shot-noise Calibration

Initial characterization of the shot noise and squeezing levels is performed using a slow photodetector and an optical spectrum analyzer (OSA) which replaces the fast detector in Fig. 4. This data is used to calibrate the shot noise of the measurement OPA and measure the squeezing generated by the squeezer OPA (See [41] supplementary). During calibration, the mechanical shutter is initially left open. As the relative delay of the squeezer path is scanned, the measurement amplifier oscillates between measuring squeezed and anti-squeezed quadratures, resulting in the black curve in Fig. 5A. The remaining pump light collected from the output is monitored on a second OSA. Because the optical coupler between the measurement and squeezer OPAs couples some of the pump used to drive the squeezer, the measurement and squeezer pumps interfere inside the measurement OPA, causing the gain, and therefore shot-noise level, of the measurement OPA to depend on ϕ . The shutter is then closed and the baseline shot noise is measured by the OSA resulting in the gray curve in Fig. 5A.

To determine the shot-noise levels corresponding to the minimum and maximum of the squeezing curve, the measurement OPA power is lowered using the VND until the measured pump power matches the minima of the pump

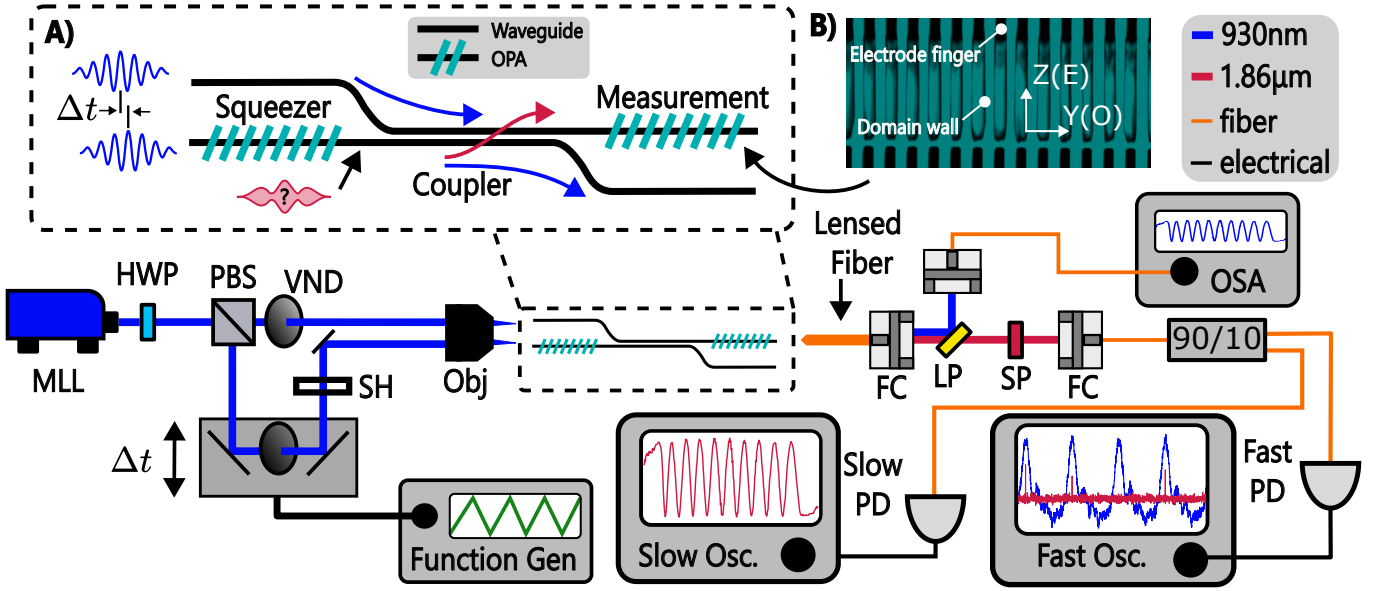


FIG. 4. Experimental setup. MLL: Titanium:sapphire tunable mode-locked laser. PBS: polarizing beamsplitter. VND: variable neutral density filter. SH: mechanical shutter. Obj: reflective objective. FC: reflective fiber collimator. LP and SP: long-pass and short-pass wavelength filters. 90/10: fiber splitter with 90% going to the fast detector and 10% going to the slow oscilloscope. PD: photodetector. Fast Osc: 80 GSPS 40 GHz oscilloscope. Slow Osc: 100 MSPS 10 MHz oscilloscope.

interference. The shot-noise minimum is then measured on the slow photodetector and OSA resulting in the red curve in Fig. 5A. This same procedure is repeated for the shot-noise maximum as well to calibrate the anti-squeezing and obtain the blue curve. The pump OSA is set to measure around 970 nm to minimize any pump depletion effects. After shot-noise calibration, the squeezing is calculated as:

$$S_{\pm}^{\phi} [dB] = 10 \log_{10} \left[\frac{\langle N(\phi) \rangle}{\langle N_{vac} \rangle} \right] \quad (9)$$

where $\langle N(\phi) \rangle$ is proportional to the current measured at the detector, and $\langle N_{vac} \rangle$ is the calibrated shot noise. We note that the variance of the measured quadrature is proportional to the average photon number for a state with zero mean field such as SV [41].

B. Slow Photodetector Measurements

Figure 5B shows the measured squeezing on the slow photodetector and OSA as a function of the input pulse energy for the squeezer waveguide with a measurement pulse energy of 30 pJ. For these measurements, the 1950-nm long-pass filter is removed to accentuate the impact of multiple modes (a Schmidt number of 2.8). Because the OSA uses a 2-nm bandpass filter, it can better suppress higher-order modes to isolate the squeezing in the fundamental mode [41, 53]. For the photodetector, the presence of higher-order modes with less squeezing reduces overall measured squeezing as the photodetector

is not mode-sensitive and measures the squeezing as averaged over all modes. At low squeezer pulse energies, the measured squeezing is limited by the gain available in the squeezer OPA and grows as the pulse energy is increased. After 5 pJ, the observed squeezing begins to decrease with increasing pulse energy. Two phenomena contribute to this behavior. First, the finite phase noise of the pump laser causes a portion of the anti-squeezed quadrature to leak into the measurement of the squeezed quadrature. Raising the squeezer gain increases the contribution of the anti-squeezing to the measurement and reduces the measured squeezing. This increased gain produces more squeezing, but the noise reduction in the squeezed quadrature is asymptotically limited by the finite efficiency of the coupler while the noise of the anti-squeezed quadrature is not (see solid theory curves in Fig. 5B). Second, nonlinear behavior in the measurement amplifier increases with input power and further degrades measured squeezing.

The solid lines plotted in Fig. 5B are calculated from the theoretical measured squeezing as a function of the coupling loss from the squeezer to measurement OPA. As SV passes through the coupler, some of the light is lost to propagation losses and fabrication imperfections in the coupler. This light is replaced with vacuum noise, causing lower squeezing and anti-squeezing values to be measured [63]. For a given measurement efficiency η , the measured squeezing can be modeled as

$$S_{\pm}^{\eta} [dB] = 10 \log_{10} [(1 - \eta) + \eta e^{\pm 2r}] \quad (10)$$

Where r is the on-chip squeezer gain in natural log

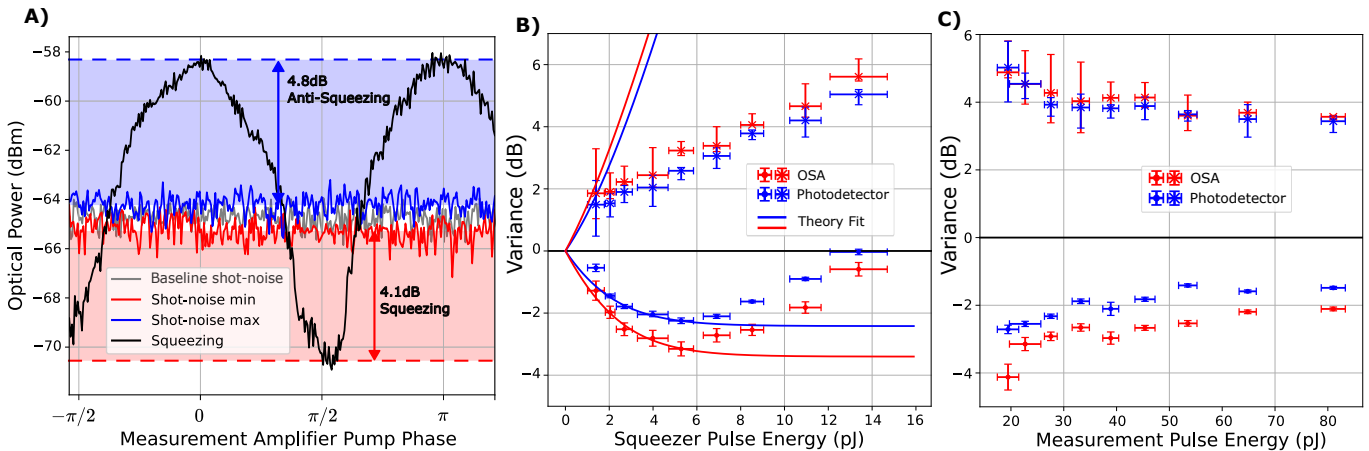


FIG. 5. A) Squeezing measurement taken on the OSA. The black curve is the amplification fringe produced from squeezed vacuum amplified by the measurement OPA. The grey curve is the baseline shot noise at the pump power used to measure the black curve. The red and blue curves are the corrected shot-noise levels to account for pump interference in the measurement OPA. B) Variance relative to vacuum vs squeezer pulse energy with a measurement pulse energy of 30 pJ. C) Variance relative to vacuum vs measurement pulse energy. Error bars are calculated from shot-noise variations during each measurement.

units. Using this fit, we estimate an effective measurement efficiency (η) of 55% at 1860 nm. This fit includes squeezing lost to inefficiencies in our coupler as well as losses to nonlinear behavior in the measurement OPA. This fitting also allows us to calculate the expected anti-squeezing, however we can see that the measured data has a stark divergence from the expected trend. This is a result of the gain compression in the measurement OPA. Because the measurement OPA operates in the pump depleted regime, the anti-squeezed vacuum cannot be sufficiently amplified to reflect the true anti-squeezing entering the OPA. The same is true for the squeezing measurements in which the shot-noise level becomes compressed, leading to lower measured squeezing.

The effects of gain depletion can also be seen in Fig. 5C which plots the measured squeezing values vs the measurement pulse energy for a fixed squeezer energy of 5 pJ. As the measurement pulse energy is decreased, the measurement OPA experiences less gain depletion, leading to higher measured squeezing and anti-squeezing. In the undepleted pump regime, measured squeezing and anti-squeezing will follow Eq.10 and remain unchanged with small changes in pump energy. Hence, we know all measurements in Fig. 5B are taken in the pump depletion regime. This is also confirmed from Fig. 2C where pump depletion effects take hold around 20 pJ. Below 20 pJ, the shot noise no longer clears the electronic noise floor of the OSA, preventing squeezing measurements at lower measurement pump energies. This problem can be mitigated by improving output coupling efficiency and operating the measurement OPA at a lower pump power.

C. Pulse-to-pulse Measurements

Fast photodetector measurements resolve the pulse-to-pulse photon number and provide the statistical information necessary to measure $P(N, \phi)$ and recover the Wigner function. Before a fast measurement, a slow measurement is conducted with the OSAs to calibrate the shot noise. During each fast measurement, the shutter is initially left open, and the fast oscilloscope is triggered using the voltage applied to the piezo driving the squeezer's delay stage to coincide with the middle of the ϕ scan. Data from the slow oscilloscope is used to determine ϕ and estimate the coupling stability based on measurement-to-measurement variations in the shot noise. After recording data, the squeezer's shutter is closed and the measurement is repeated to find the calibrated shot-noise level.

Figure 6 shows results gathered from fast photodetector measurements for a squeezer pulse energy of 5 pJ and a measurement pulse energy of 45 pJ. Sample measured histograms at 4 different phases are plotted in Fig. 6A, and each histogram corresponds to a single data point in Fig. 6B. For each measurement, we fit a 2-mode photon number distribution model to extract the variance of the fundamental mode as a function of ϕ . Figure 6B shows these measurements for three cases: slow photodetector measurements, fast photodetector measurements, and the 2-mode fit. Slow measurement values are calculated from the slow oscilloscope trace using the method outlined in section IV B. Because of the photon number offset resulting from pump depletion, the numerator and denominator of Eq.9 have a small but constant offset, resulting in the measured squeezing and anti-squeezing being underestimated. Fast measurement values are calculated using the variance of the photon numbers measured at the fast detector. This overcomes the offset problem

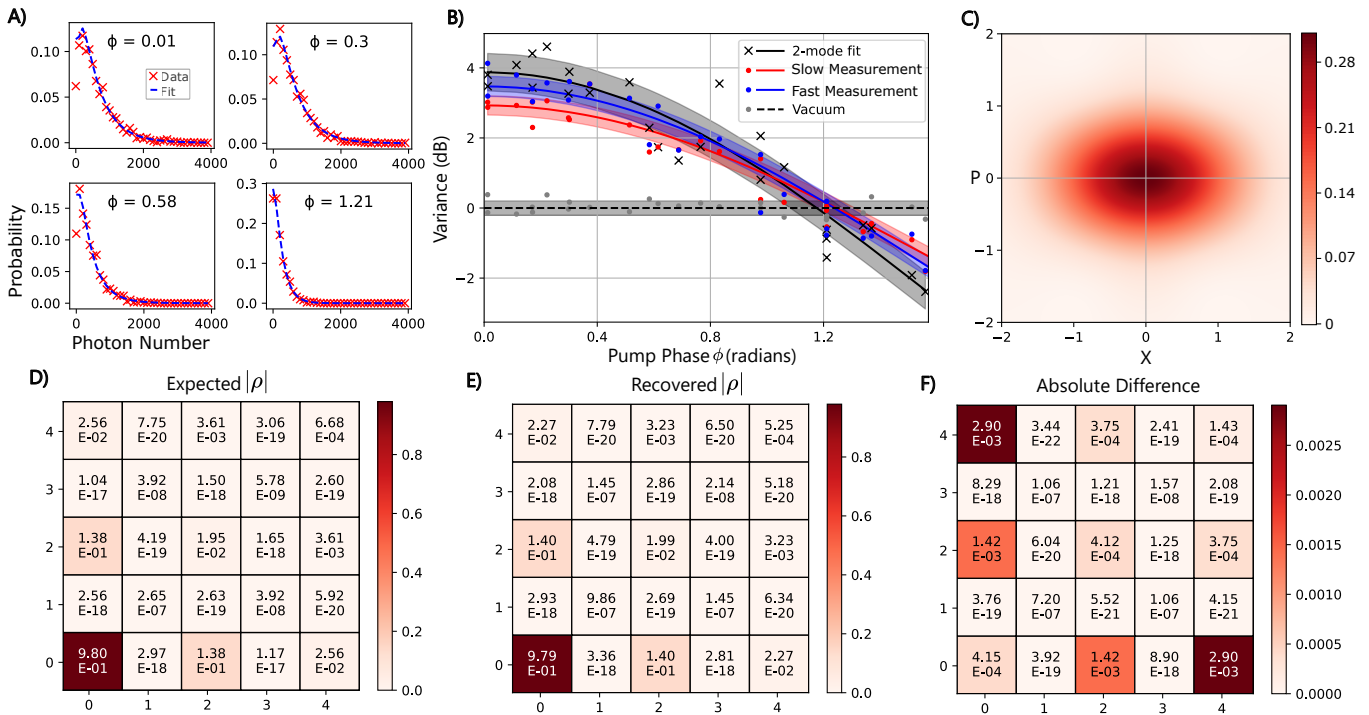


FIG. 6. A) Sample photon number distributions from fast measurements at different ϕ . Red points are data, blue curve is a 2-mode fit. B) Photon number variance vs ϕ for slow and fast (pulse-to-pulse) measurements, and the 1st mode of a 2-mode fit. C) Recovered squeezed vacuum Wigner function. D) Expected density matrix (ρ) based on measured squeezing and anti-squeezing. E) Recovered ρ . F) Absolute difference between expected and recovered ρ .

and measures more squeezing and anti-squeezing, but these measurements are still contaminated with remaining contributions from higher-order modes. The 2-mode fit addresses this problem by isolating the variance as a function of ϕ for the fundamental mode, leading to higher measured squeezing and anti-squeezing. After performing this fit for all measurements, the distributions are re-sampled and fed into a maximum likelihood algorithm which calculates the Wigner functions for squeezing data (Fig. 6C). We extract a squeezing in the fundamental mode of 2.41 ± 0.34 dB and an anti-squeezing of 3.87 ± 0.61 dB. Figure 6E shows the recovered density matrix corresponding to the Wigner function plotted in Fig. 6C. We show the expected density matrix given the measured squeezing and anti-squeezing in Fig. 6D, and the absolute difference between the expected and recovered in Fig. 6F where we calculate a fidelity of 0.9998 ± 0.0001 . While our fitting strategy limits us to states with known distributions, we can overcome this limitation with tighter bandpass filtering to better reject higher-order modes. Our losses between the chip and fiber (10 dB) and from our filter setup (6 dB) currently prevent us from tighter filtering as the remaining light is no longer strong enough to provide a sufficiently large signal-to-noise ratio at the fast photodetector.

V. CONCLUSION

We have demonstrated OPA-based Wigner tomography for squeezed vacuum in the ultrafast regime using

dispersion-engineered TFLN. The low dispersion of our OPA design allows operation with ultra-short pulses to exceed the bandwidth of homodyne measurement and access a new regime of THz repetition-rate measurement and computation. With narrower bandpass filtering at the output of our OPA and modest improvements in detection efficiency, we can perform Wigner tomography on arbitrary quantum states encoded in a femtosecond optical pulses. We show that ultrafast nanophotonic OPAs can serve as quantum measurement devices, paving the way for ultrafast quantum information processing to be realized in a room-temperature chip-scale platform.

VI. ACKNOWLEDGMENTS

Device nanofabrication was performed at the Kavli Nanoscience Institute (KNI) at Caltech. The authors gratefully acknowledge support from ARO grant no. W911NF-23-1-0048, NSF grant no. 1918549, AFOSR award FA9550-23-1-0755, DARPA award D23AP00158, the Center for Sensing to Intelligence at Caltech, the Alfred P. Sloan Foundation, and NASA/JPL.

- [1] C. L. Degen, F. Reinhard, and P. Cappellaro, Quantum sensing, *Reviews of modern physics* **89**, 035002 (2017).
- [2] N. Gisin and R. Thew, Quantum communication, *Nature photonics* **1**, 165 (2007).
- [3] H. Mark, G. Emily, N. A. of Sciences Engineering, Medicine, *et al.*, *Quantum computing: progress and prospects* (The National Academies Press, 2019).
- [4] M. Mafu and M. Senekane, Implementation and security analysis of the b92 protocol using id3100 clavis2 system, *Applied Mathematics & Information Sciences* **15**, 661 (2021).
- [5] D. Hurley-Smith and J. Hernandez-Castro, Quam bene non quantum: Identifying bias in a commercial quantum random number generator, Unpublished full-text manuscript from ResearchGate. Presented at Real World Crypto (2018).
- [6] A. Huang, S. Sajeed, P. Chaiwongkhot, M. Soucarros, M. Legré, and V. Makarov, Gap between industrial and academic solutions to implementation loopholes: testing random-gate-removal countermeasure in commercial qkd system, Unpublished full-text manuscript from Vadim Makarov (2018).
- [7] B. P. Hickam, M. He, N. Harper, S. Szoke, and S. K. Cushing, Single-photon scattering can account for the discrepancies among entangled two-photon measurement techniques, *The Journal of Physical Chemistry Letters* **13**, 4934 (2022), pMID: 35635002, <https://doi.org/10.1021/acs.jpcllett.2c00865>.
- [8] E. Pavel, S. Jinga, B. Vasile, A. Dinescu, V. Marinescu, R. Trusca, and N. Tosa, Quantum optical lithography from 1 nm resolution to pattern transfer on silicon wafer, *Optics & Laser Technology* **60**, 80 (2014).
- [9] A. F. Abouraddy, M. B. Nasr, B. E. Saleh, A. V. Sergienko, and M. C. Teich, Quantum-optical coherence tomography with dispersion cancellation, *Physical Review A* **65**, 053817 (2002).
- [10] H. Defienne, W. P. Bowen, M. Chekhova, G. B. Lemos, D. Oron, S. Ramelow, N. Treps, and D. Faccio, Advances in quantum imaging, *Nature Photonics* , 1 (2024).
- [11] V. Hassija, V. Chamola, V. Saxena, V. Chanana, P. Parashari, S. Mumtaz, and M. Guizani, Present landscape of quantum computing, *IET Quantum Communication* **1**, 42 (2020).
- [12] G. A. Quantum, Collaborators*†, F. Arute, K. Arya, R. Babbush, D. Bacon, J. C. Bardin, R. Barends, S. Boixo, M. Broughton, B. B. Buckley, *et al.*, Harteefock on a superconducting qubit quantum computer, *Science* **369**, 1084 (2020).
- [13] F. Acasiete, F. P. Agostini, J. K. Moqadam, and R. Portugal, Implementation of quantum walks on ibm quantum computers, *Quantum Information Processing* **19**, 1 (2020).
- [14] L. Thylén and L. Wosinski, Integrated photonics in the 21st century, *Photonics Research* **2**, 75 (2014).
- [15] L. Ledezma, R. Sekine, Q. Guo, R. Nehra, S. Jahani, and A. Marandi, Intense optical parametric amplification in dispersion-engineered nanophotonic lithium niobate waveguides, *Optica* **9**, 303 (2022).
- [16] C. Leefmans, A. Dutt, J. Williams, L. Yuan, M. Parto, F. Nori, S. Fan, and A. Marandi, Topological dissipation in a time-multiplexed photonic resonator network, *Nature Physics* **18**, 442 (2022).
- [17] S. Konno, W. Asavanant, F. Hanamura, H. Nagayoshi, K. Fukui, A. Sakaguchi, R. Ide, F. China, M. Yabuno, S. Miki, *et al.*, Propagating gottesman-kitaev-preskill states encoded in an optical oscillator, arXiv preprint arXiv:2309.02306 (2023).
- [18] S. Konno, W. Asavanant, F. Hanamura, H. Nagayoshi, K. Fukui, A. Sakaguchi, R. Ide, F. China, M. Yabuno, S. Miki, *et al.*, Logical states for fault-tolerant quantum computation with propagating light, *Science* **383**, 289 (2024).
- [19] R. Whittaker, C. Erven, A. Neville, M. Berry, J. O'Brien, H. Cable, and J. Matthews, Absorption spectroscopy at the ultimate quantum limit from single-photon states, *New Journal of Physics* **19**, 023013 (2017).
- [20] L.-C. Kwек, L. Cao, W. Luo, Y. Wang, S. Sun, X. Wang, and A. Q. Liu, Chip-based quantum key distribution, *AAPPS Bulletin* **31**, 1 (2021).
- [21] X.-T. Fang, P. Zeng, H. Liu, M. Zou, W. Wu, Y.-L. Tang, Y.-J. Sheng, Y. Xiang, W. Zhang, H. Li, *et al.*, Implementation of quantum key distribution surpassing the linear rate-transmittance bound, *Nature Photonics* **14**, 422 (2020).
- [22] S.-K. Liao, W.-Q. Cai, W.-Y. Liu, L. Zhang, Y. Li, J.-G. Ren, J. Yin, Q. Shen, Y. Cao, Z.-P. Li, *et al.*, Satellite-to-ground quantum key distribution, *Nature* **549**, 43 (2017).
- [23] M. Okano, H. H. Lim, R. Okamoto, N. Nishizawa, S. Kurimura, and S. Takeuchi, 0.54 μm resolution two-photon interference with dispersion cancellation for quantum optical coherence tomography, *Scientific reports* **5**, 18042 (2015).
- [24] H.-S. Zhong, H. Wang, Y.-H. Deng, M.-C. Chen, L.-C. Peng, Y.-H. Luo, J. Qin, D. Wu, X. Ding, Y. Hu, *et al.*, Quantum computational advantage using photons, *Science* **370**, 1460 (2020).
- [25] B. J. Lawrie, P. D. Lett, A. M. Marino, and R. C. Pooser, Quantum sensing with squeezed light, *Acs Photonics* **6**, 1307 (2019).
- [26] L. McCuller, C. Whittle, D. Ganapathy, K. Komori, M. Tse, A. Fernandez-Galiana, L. Barsotti, P. Fritschel, M. MacInnis, F. Matichard, *et al.*, Frequency-dependent squeezing for advanced ligo, *Physical review letters* **124**, 171102 (2020).
- [27] W. Asavanant, Y. Shiozawa, S. Yokoyama, B. Charoensombutamon, H. Emura, R. N. Alexander, S. Takeda, J.-i. Yoshikawa, N. C. Menicucci, H. Yonezawa, *et al.*, Generation of time-domain-multiplexed two-dimensional cluster state, *Science* **366**, 373 (2019).
- [28] M. V. Larsen, X. Guo, C. R. Breum, J. S. Neergaard-Nielsen, and U. L. Andersen, Deterministic generation of a two-dimensional cluster state, *Science* **366**, 369 (2019).
- [29] L. Serino, W. Ridder, A. Bhattacharjee, J. Gil-Lopez, B. Brecht, and C. Silberhorn, Orchestrating time and color: a programmable source of high-dimensional entanglement, *Optica Quantum* **2**, 339 (2024).
- [30] A. Eckstein, B. Brecht, and C. Silberhorn, A quantum pulse gate based on spectrally engineered sum frequency generation, *Optics express* **19**, 13770 (2011).
- [31] V. Ansari, G. Harder, M. Allgaier, B. Brecht, and C. Silberhorn, Temporal-mode measurement tomography of a quantum pulse gate, *Physical Review A* **96**, 063817

- (2017).
- [32] J. Roslund, R. M. De Araujo, S. Jiang, C. Fabre, and N. Treps, Wavelength-multiplexed quantum networks with ultrafast frequency combs, *Nature Photonics* **8**, 109 (2014).
- [33] R. Nehra, A. Win, M. Eaton, R. Shahrokhshahi, N. Sridhar, T. Gerrits, A. Lita, S. W. Nam, and O. Pfister, State-independent quantum state tomography by photon-number-resolving measurements, *Optica* **6**, 1356 (2019).
- [34] K. Laiho, K. N. Cassemiro, D. Gross, and C. Silberhorn, Probing the negative wigner function of a pulsed single photon point by point, *Physical review letters* **105**, 253603 (2010).
- [35] K. Takase, J.-i. Yoshikawa, W. Asavanant, M. Endo, and A. Furusawa, Generation of optical schrödinger cat states by generalized photon subtraction, *Physical Review A* **103**, 013710 (2021).
- [36] T. Gerrits, S. Glancy, T. S. Clement, B. Calkins, A. E. Lita, A. J. Miller, A. L. Migdall, S. W. Nam, R. P. Mirin, and E. Knill, Generation of optical coherent-state superpositions by number-resolved photon subtraction from the squeezed vacuum, *Physical Review A* **82**, 031802 (2010).
- [37] J.-i. Yoshikawa, W. Asavanant, and A. Furusawa, Purification of photon subtraction from continuous squeezed light by filtering, *Physical Review A* **96**, 052304 (2017).
- [38] D. V. Sychev, A. E. Ulanov, A. A. Pushkina, M. W. Richards, I. A. Fedorov, and A. I. Lvovsky, Enlargement of optical schrödinger’s cat states, *Nature Photonics* **11**, 379 (2017).
- [39] N. Takanashi, A. Inoue, T. Kashiwazaki, T. Kazama, K. Enbutsu, R. Kasahara, T. Umeki, and A. Furusawa, All-optical phase-sensitive detection for ultra-fast quantum computation, *Optics Express* **28**, 34916 (2020).
- [40] Y. Shaked, Y. Michael, R. Z. Vered, L. Bello, M. Rosenbluh, and A. Pe’er, Lifting the bandwidth limit of optical homodyne measurement with broadband parametric amplification, *Nature communications* **9**, 609 (2018).
- [41] R. Nehra, R. Sekine, L. Ledezma, Q. Guo, R. M. Gray, A. Roy, and A. Marandi, Few-cycle vacuum squeezing in nanophotonics, *Science* **377**, 1333 (2022).
- [42] M. Kalash and M. V. Chekhova, Wigner function tomography via optical parametric amplification, *Optica* **10**, 1142 (2023).
- [43] C. M. Caves, Quantum-mechanical noise in an interferometer, *Physical Review D* **23**, 1693 (1981).
- [44] A. M. Marino, N. Corzo Trejo, and P. D. Lett, Effect of losses on the performance of an su (1, 1) interferometer, *Physical Review A—Atomic, Molecular, and Optical Physics* **86**, 023844 (2012).
- [45] A. Inoue, T. Kashiwazaki, T. Yamashima, N. Takanashi, T. Kazama, K. Enbutsu, K. Watanabe, T. Umeki, M. Endo, and A. Furusawa, Toward a multi-core ultrafast optical quantum processor: 43-GHz bandwidth real-time amplitude measurement of 5-dB squeezed light using modularized optical parametric amplifier with 5G technology, *Applied Physics Letters* **122**, 104001 (2023).
- [46] G. Frascella, E. E. Mikhailov, N. Takanashi, R. V. Zakharov, O. V. Tikhonova, and M. V. Chekhova, Wide-field su(1,1) interferometer, *Optica* **6**, 1233 (2019).
- [47] F. Hudelist, J. Kong, C. Liu, J. Jing, Z. Ou, and W. Zhang, Quantum metrology with parametric amplifier-based photon correlation interferometers, *Nature communications* **5**, 3049 (2014).
- [48] M. L. Marable, S.-K. Choi, and P. Kumar, Measurement of quantum-noise correlations in parametric image amplification, *Optics Express* **2**, 84 (1998).
- [49] Y. Sun, H. Tu, S. You, C. Zhang, Y.-Z. Liu, and S. A. Boppart, Detection of weak near-infrared optical imaging signals under ambient light by optical parametric amplification, *Optics letters* **44**, 4391 (2019).
- [50] T. Yamashima, T. Kashiwazaki, T. Suzuki, R. Nehra, T. Nakamura, A. Inoue, T. Umeki, K. Takase, W. Asavanant, M. Endo, *et al.*, All-optical measurement-device-free feedforward enabling ultra-fast quantum information processing, arXiv preprint arXiv:2410.20693 (2024).
- [51] I. Barakat, M. Kalash, D. Scharwald, P. Sharapova, N. Lindlein, and M. Chekhova, Simultaneous measurement of multimode squeezing through multimode phase-sensitive amplification, *Optica Quantum* **3**, 36 (2025).
- [52] A. B. U’Ren, C. Silberhorn, R. Erdmann, K. Banaszek, W. P. Grice, I. A. Walmsley, and M. G. Raymer, Generation of pure-state single-photon wavepackets by conditional preparation based on spontaneous parametric downconversion, arXiv preprint quant-ph/0611019 (2006).
- [53] M. Houde and N. Quesada, Waveguided sources of consistent, single-temporal-mode squeezed light: The good, the bad, and the ugly, *AVS Quantum Science* **5** (2023).
- [54] J. Flórez, J. S. Lundeen, and M. V. Chekhova, Pump depletion in parametric down-conversion with low pump energies, *Optics Letters* **45**, 4264 (2020).
- [55] N. Lordi, E. J. Tsao, A. J. Lind, S. A. Diddams, and J. Combes, Quantum theory of temporally mismatched homodyne measurements with applications to optical-frequency-comb metrology, *Physical Review A* **109**, 033722 (2024).
- [56] W. Bidle, Optical quantum state tomography, Department of Physics & Astronomy (2023).
- [57] W. Wasilewski, A. I. Lvovsky, K. Banaszek, and C. Radzewicz, Pulsed squeezed light: Simultaneous squeezing of multiple modes, *Physical Review A—Atomic, Molecular, and Optical Physics* **73**, 063819 (2006).
- [58] J. Williams, R. Nehra, E. Sendonaris, L. Ledezma, R. M. Gray, R. Sekine, and A. Marandi, Ultrashort pulse biphoton source in lithium niobate nanophotonics at 2 μm , *Nanophotonics* (2024).
- [59] Q. Guo, R. Sekine, L. Ledezma, R. Nehra, D. J. Dean, A. Roy, R. M. Gray, S. Jahani, and A. Marandi, Femtojoule femtosecond all-optical switching in lithium niobate nanophotonics, *Nature Photonics* **16**, 625 (2022).
- [60] G. H. Li, R. Sekine, R. Nehra, R. M. Gray, L. Ledezma, Q. Guo, and A. Marandi, All-optical ultrafast relu function for energy-efficient nanophotonic deep learning, *Nanophotonics* **12**, 847 (2023).
- [61] R. Sekine, R. M. Gray, L. Ledezma, S. Zhou, Q. Guo, and A. Marandi, Multi-octave frequency comb from an ultra-low-threshold nanophotonic parametric oscillator, arXiv preprint arXiv:2309.04545 (2023).
- [62] K. Chinni and N. Quesada, Beyond the parametric approximation: Pump depletion, entanglement, and squeezing in macroscopic down-conversion, *Physical Review A* **110**, 013712 (2024).
- [63] C. H. Henry and R. F. Kazarinov, Quantum noise in photonics, *Reviews of Modern Physics* **68**, 801 (1996).

Supplementary Information for Ultrafast All-Optical Measurement of Squeezed Vacuum in a Lithium Niobate Nanophotonic Circuit

James Williams¹, Elina Sendonaris², Rajveer Nehra^{1,3,4,5}, Robert M Gray¹,
Ryoto Sekine¹, Alireza Marandi^{1,2}

February 6, 2025

¹ Department of Electrical Engineering, California Institute of Technology, Pasadena, California 91125
² Department of Applied Physics, California Institute of Technology, Pasadena, California 91125
³ Department of Electrical and Computer Engineering, University of Massachusetts Amherst, Amherst, Massachusetts 01003, USA
⁴ Department of Physics, University of Massachusetts Amherst, Amherst, Massachusetts 01003, USA
⁵ College of Information and Computer Science, University of Massachusetts Amherst, Amherst, Massachusetts 01003, USA

1 Multimode Cascaded Squeezing in the Heisenberg picture

We use the formalism of [wasilewski2006pulsed] to derive the output of a two cascaded multimode OPAs: a squeezer OPA and a measurement OPA. Figure 1 shows the circuit diagram. We begin with the state after the squeezer OPA (denoted with superscript s) and decompose the annihilation operator into the squeezer OPA's eigenmodes (denoted by subscript m):

$$\begin{aligned}\hat{a}^s(t) &= \sum_m \psi_m^{s*}(t) \hat{a}_m^s \\ &= \sum_m \psi_m^{s*}(t) (\cosh r_m^s \hat{a}_m^{in} + \sinh r_m^s \hat{a}_m^{in\dagger})\end{aligned}\quad (1)$$

where r_m^s is the squeezing parameter of mode m . Each eigenmode of the squeezer OPA is independently squeezed. To simplify later expressions, we assume that $r_m^s = r_m^s(\phi)$ where ϕ is the phase of the squeezed vacuum relative to the measurement pump. In our experiment, we inject vacuum into the squeezer OPA, and so $\hat{a}^{in} \equiv \hat{a}^{vac}$.

After the squeezer OPA, the state is placed into the measurement OPA (superscript ms and mode subscript n) and the resulting output operator is labeled $\hat{a}^{out}(t)$. The measurement OPA amplifies its own modes as independent single-mode OPAs:

$$\begin{aligned}\hat{a}^{out}(t) &= \sum_n \psi_n^{ms*}(t) \hat{a}_n^{out} \\ &= \sum_n \psi_n^{ms*}(t) (\cosh r_n^{ms} \hat{a}_n^s + \sinh r_n^{ms} \hat{a}_n^{s\dagger})\end{aligned}\quad (2)$$

We can write the squeezed operators in the measurement OPA basis as a function of the mode overlaps between the measurement OPA's and squeezer OPA's eigenmodes $\sigma_{mn} = \int dt \psi_n^{ms}(t) \psi_m^{s*}(t)$

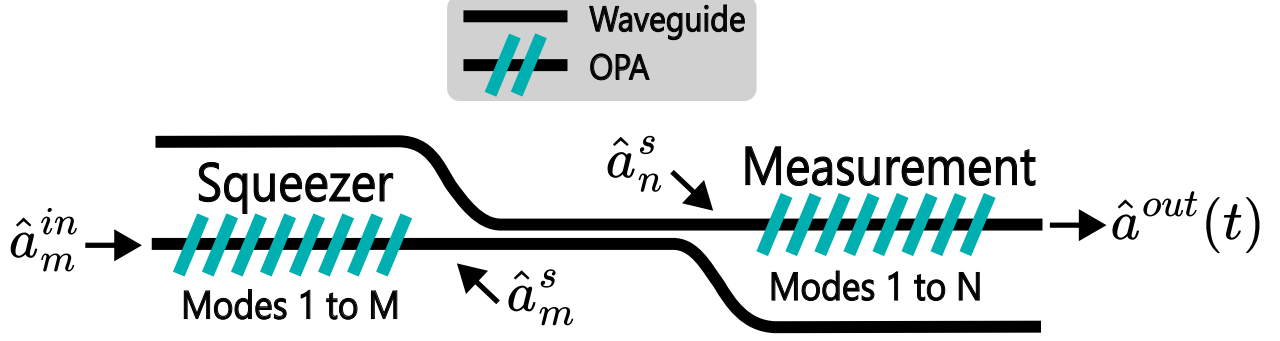


Figure 1: A diagram of the squeezer and measurement OPA circuit.

$$\begin{aligned}
\hat{a}_n^s &= \int_{-\infty}^{\infty} dt \psi_n^{ms}(t) \hat{a}^s(t) \\
&= \int_{-\infty}^{\infty} dt \psi_n^{ms}(t) \sum_m \psi_m^{s*}(t) \hat{a}_m^s \\
&= \sum_m \sigma_{mn} \hat{a}_m^s.
\end{aligned} \tag{3}$$

The output annihilation operator is then

$$\begin{aligned}
\hat{a}^{out}(t) &= \sum_{mn} \psi_n^{ms*}(t) (\cosh r_n^{ms} \sigma_{mn} \hat{a}_m^s + \sinh r_n^{ms} \sigma_{mn}^* \hat{a}_m^{s\dagger}) \\
&= \sum_{mn} \psi_n^{ms*}(t) (\cosh r_n^{ms} \sigma_{mn} (\cosh r_m^s \hat{a}_m^{in} + \sinh r_m^s \hat{a}_m^{in\dagger}) \\
&\quad + \sinh r_n^{ms} \sigma_{mn}^* (\cosh r_m^s \hat{a}_m^{in\dagger} + \sinh r_m^s \hat{a}_m^{in}))
\end{aligned} \tag{4}$$

For large measurement OPA gains, we use the approximation $\cosh r_n^{ms} \approx \sinh r_n^{ms} \approx \frac{1}{2} \exp(r_n^{ms})$, when $e^{r^{ms}} \gg 1 \gg e^{-r^{ms}}$. Then, the output operator becomes:

$$\hat{a}^{out}(t) = \sum_{mn} \frac{e^{r_n^{ms}}}{2} \psi_n^{ms*}(t) (\sigma_{mn} (\cosh r_m^s \hat{a}_m^{in} + \sinh r_m^s \hat{a}_m^{in\dagger}) + \sigma_{mn}^* (\cosh r_m^s \hat{a}_m^{in\dagger} + \sinh r_m^s \hat{a}_m^{in})) \tag{5}$$

We can write the photon number operator for an individual pulse as

$$\begin{aligned}
\hat{N} &= \int_{-\Delta t}^{\Delta t} dt \hat{a}^{out\dagger}(t) \hat{a}^{out}(t) \\
&= \int dt \sum_{m,m',n,n'} \frac{e^{r_n^{ms} + r_{n'}^{ms}}}{4} \left(\psi_n^{ms}(t) (\sigma_{mn}^* (\cosh r_m^s \hat{a}_m^{in\dagger} + \sinh r_m^s \hat{a}_m^{in}) \right. \\
&\quad \left. + \sigma_{mn} (\cosh r_m^s \hat{a}_m^{in} + \sinh r_m^s \hat{a}_m^{in\dagger})) \right) \\
&\quad \left(\psi_{n'}^{ms*}(t) (\sigma_{m'n'} (\cosh r_{m'}^s \hat{a}_{m'}^{in} + \sinh r_{m'}^s \hat{a}_{m'}^{in\dagger}) \right. \\
&\quad \left. + \sigma_{m'n'}^* (\cosh r_{m'}^s \hat{a}_{m'}^{in\dagger} + \sinh r_{m'}^s \hat{a}_{m'}^{in})) \right) \\
&= \sum_{m,n} e^{2r_n^{ms}} (\text{Re}[\sigma_{mn}] e^{r_m^s} \hat{x}_m^{in} - \text{Im}[\sigma_{mn}] e^{-r_m^s} \hat{y}_m^{in})^2
\end{aligned} \tag{6}$$

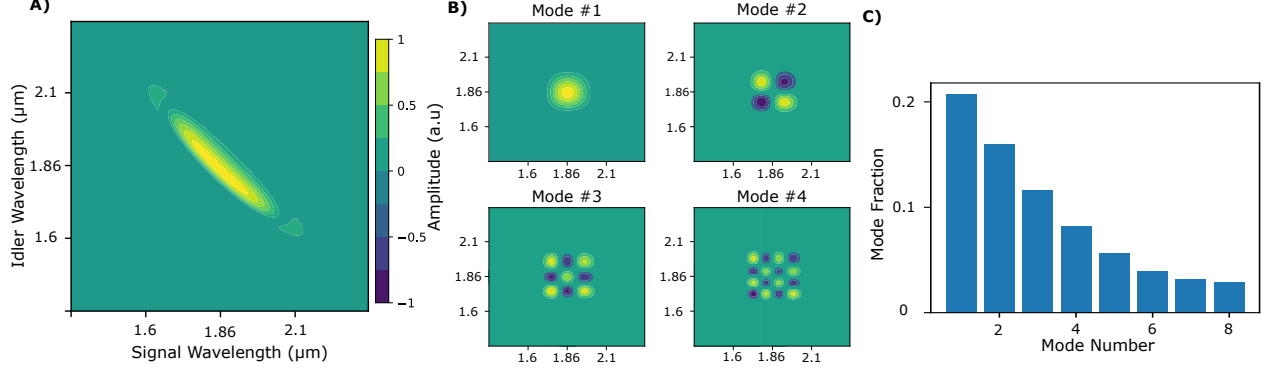


Figure 2: A) A plot of the joint-spectral intensity function of the squeezed vacuum produced by our OPA. B) The first four modes of the JSI calculated via the Bloch-Messiah decomposition. C) Plot of the mode number vs proportion of mode present in the JSI.

where the integral over Δt captures the total time-duration of the pulse, and we have used the orthonormality of modes ($\int dt \psi_n(t)\psi_{n'}^*(t) = \delta_{nn'}$) to insert $\delta_{nn'}$ and $\delta_{mm'}$ and resolve m' and n' in the summation.

Bandpass filtering around degeneracy suppresses the imaginary component of σ_{mn} as imaginary contributions arise from phase walk-off in the JSI away from degeneracy. Taking $\text{Im}[\sigma_{mn}]e^{-r_m^s} \ll \text{Re}[\sigma_{mn}]e^{r_m^s}$, we have:

$$\hat{N} = \sum_{m,n} \frac{e^{2r_n^{ms}+2r_m^s}}{4} \sigma_{mn} (\hat{a}_m^{in} + \hat{a}_m^{in\dagger})^2, \quad (7)$$

If we take a compare to the case of no squeezing from the squeezer OPA ($\sigma_{mn} = \delta_{mn}, r_m^s = 0 \forall m$),

$$\hat{N} = \sum_n \frac{e^{2r_n^{ms}}}{4} (\hat{a}_n^{in} + \hat{a}_n^{in\dagger})^2 \quad (8)$$

and assume M squeezer modes and N measurement modes, we show that there are now MN modes with effective squeezing parameters $r_{m,n}^{eff} = r_n^{ms} + r_m^s$, whose contributions are weighted by σ_{mn} . From here, we can use the quadrature $\hat{X} = \frac{1}{\sqrt{2}}(\hat{a} + \hat{a}^\dagger)$ to re-write Eq.7 as

$$\hat{N} = \sum_{m,n} \frac{e^{2r_n^{ms}+2r_m^s}}{8} \sigma_{mn} (\hat{X}_m^{in})^2 \quad (9)$$

In our experiment, we make the assumption that only the first two modes provide significant contributions to the measured statistics as our Schmidt number after filtering is 1.35, and so we truncate m and n to the range [1,2]. Furthermore, we know that σ_{mn} where m and n are of different parity are zero. This simplifies Eq.9 to:

$$\hat{N} = \frac{e^{2r_1^{ms}+2r_1^s}}{8} \sigma_{11} (\hat{X}_1^{in})^2 + \frac{e^{2r_2^{ms}+2r_2^s}}{8} \sigma_{22} (\hat{X}_2^{in})^2 \quad (10)$$

This allows us to model the measured photon number distribution as the sum of two independent photon number distributions. During the experiment, we treat the fast photodetector as a macroscopic photon number resolving detector such that $N \propto I_d$ where I_d is the current measured on the detector integrated over a single pulse. For a single mode, the photon number distribution is [kalash'wigner'2023]:

$$P_{\langle N \rangle}^1(N, r) = \frac{1}{\sqrt{2\pi N \langle N \rangle(r)}} e^{-\frac{N}{2\langle N \rangle(r)}} \quad (11)$$

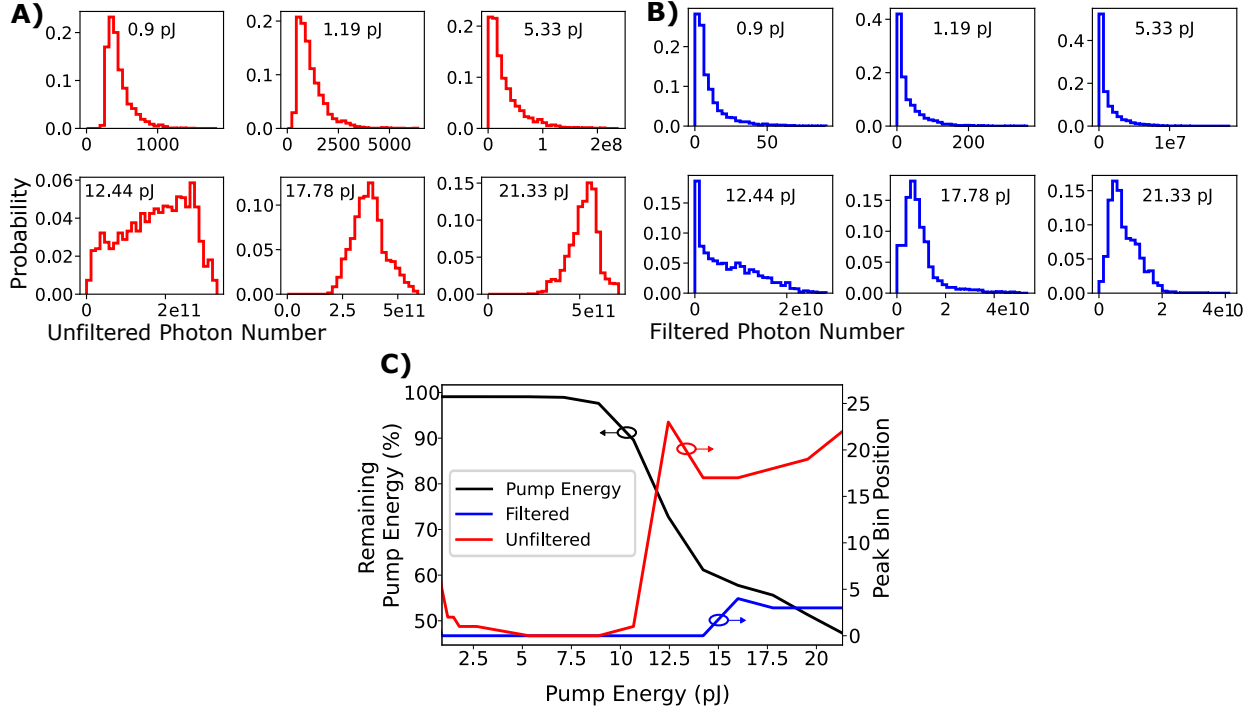


Figure 3: A) Simulated photon number distributions for unfiltered detection across different pump energies. B) Simulated photon number distributions for 20-nm bandpass filtered detection across different pump energies. C) A plot of the remaining pump energy after pulse propagation (lower remaining energy is a more depleted pump), and the peak histogram bin for the unfiltered and filtered simulations.

with average photon number $\langle N \rangle(r) = e^{2r}/4$. Since the photon number contributions from each mode are summed at the detector, we can model the total distribution as the convolution of two single-mode distributions, i.e:

$$P^2(N, r) = \int_0^\infty P_{\langle N_1 \rangle}^1(N - n, r) P_{\langle N_2 \rangle}^1(n, r) dn \quad (12)$$

By fitting Eq.12 to the measured photon number distributions, we isolate the squeezing parameter of the 1st mode from higher-order modes.

2 Calculation of the Joint Spectral Intensity and its Modes

Figure 2A shows the joint-spectral intensity function (JSI) of the squeezed vacuum we measure. We calculate our JSI using the dispersive parameters obtained from mode simulations, the input pump pulse energy, and the resources from [houde2023waveguided]. The modes of the JSI are found by performing the Bloch-Messiah decomposition which calculates the modes such that the correlations between pairs of modes are minimized. The first four modes are plotted in Fig. 2B and the fraction of the first eight modes comprising the JSI is shown in Fig. 2C. The JSI decomposition reveals a Schmidt mode number of 7.1. This same calculation can be repeated for the measurement OPA resulting in a Schmidt number of 3.9. Filtering before detection reduces this number to 1.35.

3 Pump Depletion in Simulation

As discussed in the main text, we model the effects of pump depletion as a shift in the peak of the photon number distribution. Figure 3 shows semi-classical simulation results of vacuum amplification in our OPA

generated via a split-step Fourier method. As pump energy increases, the pump pulse depletes more efficiently given the peak-power-enhanced nonlinear interaction, and causes the peak of $P(N)$ to shift away from 0. Fig. 3B shows simulated $P(N)$ with 20-nm bandpass filtering at degeneracy before measurement. In this case, the dominant contribution to the peak shift is pump depletion as multimode effects are suppressed. The difference can be seen in Fig. 3A where in the unfiltered case, peak shifting is more prominent thanks to strong multimode contributions. Peak shifting as a result of pump depletion has recently been studied in single-mode quantum simulations [[chinni2024beyond](#)] and experimentally observed [[florez2020pump](#)].